Aalto University School of Engineering
CFD-group/ Department of Applied Mechanics

MEMO No CFD/MECHA-8-2011 DATE: March 30, 2011

TITLE

Time-Accurate Simulations of a Single-Channel Sevage Pump

AUTHOR(S)
Juhaveikko Ala-Juusela

ABSTRACT

A single-blade sewage pump is simulated numerically using a FINFLO flow solver. A low-Reynolds number approach is utilized with a $k-\epsilon$ and a $k-\omega$ turbulence closure. Simulations are done with two grid densities and also utilizing both preconditioning and pressure correction methods for one case.

MAIN RESULT

Pump head, efficiency and torque are obtained from the simulated flow field and compared to measured data. The velocity distributions are also compared to the measurements.

PAGES
34

KEY WORDS
FINFLO, $k-\epsilon$ model, $k-\omega$ model, pump performance

APPROVED BY

Timo Siikonen March 30, 2011

Contents

Nomenclature

C	model coefficient in $k-\omega$ turbulence model
C_p	pressure coefficient
E	total energy
F, G, H	flux vectors in the x-, y- and z-directions
H	total head
Pr	Prandtl number
Q	source term vector
Re	Reynolds number
T	temperature
U	vector of conservative variables
V	velocity vector
c_p	specific heat at a constant pressure
c_v	specific heat at a constant volume
e	specific internal energy
k	turbulent kinetic energy
$\dot{m}$	mass flow
p	pressure
$\vec{q}$	heat flux
t	time
u, v, w	velocity components in the x-, y- and z-directions
u_τ	friction velocity $(= \sqrt{\tau_w/\rho})$
y^+	dimensionless distance from the wall $(= yu_\tau/\nu)$
β	artificial compressibility coefficient, model constants in the $k-\omega$ model
δ_{ij}	Kronecker's delta
ϵ	dissipation of the kinetic energy of the turbulence
θ	temperature difference $(= T - T_\infty)$
μ	dynamic viscosity
ν	kinematic viscosity
ϕ	scalar
ρ	density
τ	shear stress
ω	specific dissipation rate of turbulent kinetic energy $(= \epsilon/(\beta^* k))$

Superscripts

T	transposition
l	left side
r	right side
w	wall value
$'$	fluctuating component

Subscripts

T	turbulent
i, j, k	$i-$, $j-$ k-component
t	tangential component
n	normal component

1 Introduction

In this study a single-channel sewage pump is simulated numerically using FINFLO flow solver. Two different grid densities are used, in a coarser one, every second grid point of the denser one is used. A low-Reynolds number $k-\epsilon$ and $k-\omega$ turbulence models are utilized in the simulations. Denser $k-\omega$-simulation is also made using pressure correction as a solution method in addition to the traditional preconditioning.

In the following, the governing equations and turbulence modelling are firstly described. Next, the computational domain and the grid are depicted and, finally, the results of the simulation are presented and compared to measurements.

2 Flow Equations

A low-Reynolds number approach is used in FINFLO. The Reynolds-averaged Navier-Stokes equations, and the equations for the kinetic energy (k) and dissipation (ϵ) of turbulence can be written in the following form

$$\frac{\partial U}{\partial t}+\frac{\partial (F-F_v)}{\partial x}+\frac{\partial (G-G_v)}{\partial y}+\frac{\partial (H-H_v)}{\partial z}=Q \tag{1}$$

where the unknowns are $U=(\rho,\rho u,\rho v,\rho w,E,\rho k,\rho\epsilon)^T$. The inviscid fluxes are

$$F=\begin{pmatrix}\rho u\\ \rho u^2+p+\frac{2}{3}\rho k\\ \rho vu\\ \rho wu\\ (E+p+\frac{2}{3}\rho k)u\\ \rho uk\\ \rho u\epsilon\end{pmatrix}\quad G=\begin{pmatrix}\rho v\\ \rho uv\\ \rho v^2+p+\frac{2}{3}\rho k\\ \rho wv\\ (E+p+\frac{2}{3}\rho k)v\\ \rho vk\\ \rho v\epsilon\end{pmatrix}\quad H=\begin{pmatrix}\rho w\\ \rho uw\\ \rho vw\\ \rho w^2+p+\frac{2}{3}\rho k\\ (E+p+\frac{2}{3}\rho k)w\\ \rho wk\\ \rho w\epsilon\end{pmatrix} \tag{2}$$

where ρ is the density, the velocity vector by using Cartesian components is $\vec{V}=u\vec{i}+v\vec{j}+w\vec{k}$, p is the pressure, k is the turbulent kinetic energy and ϵ its dissipation, and the total energy E is defined as

$$E=\rho e+\frac{\rho\vec{V}\cdot\vec{V}}{2}+\rho k \tag{3}$$

where e is the specific internal energy. The viscous fluxes are

$$F_v=\begin{pmatrix}0\\ \tau_{xx}\\ \tau_{xy}\\ \tau_{xz}\\ u\tau_{xx}+v\tau_{xy}+w\tau_{xz}-q_x\\ \mu_k(\partial k/\partial x)\\ \mu_\epsilon(\partial\epsilon/\partial x)\end{pmatrix}\quad G_v=\begin{pmatrix}0\\ \tau_{xy}\\ \tau_{yy}\\ \tau_{yz}\\ u\tau_{xy}+v\tau_{yy}+w\tau_{yz}-q_y\\ \mu_k(\partial k/\partial y)\\ \mu_\epsilon(\partial\epsilon/\partial y)\end{pmatrix}$$

$$H_v = \begin{pmatrix} 0 \\ \tau_{xz} \\ \tau_{yz} \\ \tau_{zz} \\ u\tau_{xz} + v\tau_{yz} + w\tau_{zz} - q_z \\ \mu_k(\partial k/\partial z) \\ \mu_\epsilon(\partial \epsilon/\partial z) \end{pmatrix} \tag{4}$$

Here the stress tensor, τ_{ij}, includes laminar and turbulent components. The fluid is assumed to be Newtonian and, therefore, the laminar stresses are modelled by using Stokes hypothesis. The Reynolds stresses $\overline{\rho u_i'' u_j''}$ are included in the stress tensor τ_{ij}.

$$\tau_{ij} = \mu \left[\frac{\partial u_j}{\partial x_i} + \frac{\partial u_i}{\partial x_j} - \frac{2}{3}(\nabla \cdot \vec{V})\delta_{ij} \right] - \overline{\rho u_i'' u_j''} + \frac{2}{3}\rho k \delta_{ij} \tag{5}$$

For the Reynolds stresses, Boussinesq's approximation

$$-\overline{\rho u_i'' u_j''} = \mu_T \left[\frac{\partial u_j}{\partial x_i} + \frac{\partial u_i}{\partial x_j} - \frac{2}{3}(\nabla \cdot \vec{V})\delta_{ij} \right] - \frac{2}{3}\rho k \delta_{ij} \tag{6}$$

is utilized. Here μ_T is a turbulent viscosity coefficient, which is calculated by using a turbulence model, and δ_{ij} is the Kronecker's delta. In the momentum and energy equations, the kinetic energy contribution $2/3\rho k\delta_{ij}$ has been connected with pressure and appears in the convective fluxes, whereas the diffusive part is connected with the viscous fluxes. The viscous stresses contains a laminar and a turbulent parts. The heat flux can be written as

$$\vec{q} = -(\lambda + \lambda_T)\nabla T = -\left(\mu \frac{c_p}{Pr} + \mu_T \frac{c_p}{Pr_T} \right) \nabla T \tag{7}$$

where λ is a molecular and λ_T a turbulent thermal conductivity coefficient and Pr is a laminar and Pr_T a turbulent Prandtl number, and c_p is a specific heat at constant pressure. The diffusion of turbulence variables is modelled as

$$\mu_k \nabla k = \left(\mu + \frac{\mu_T}{\sigma_k} \right) \nabla k \tag{8}$$

$$\mu_\epsilon \nabla \epsilon = \left(\mu + \frac{\mu_T}{\sigma_\epsilon} \right) \nabla \epsilon \tag{9}$$

where σ_k and σ_ϵ are turbulent Schmidt's numbers of k and ϵ, respectively. Density is obtained from an equation of state $p = p(\rho, T)$ Since this case is essentially incompressible, pressure differences $p - p_0$ are solved instead of pressure. The components of the source term Q are non-zero in possible buoyancy terms and in turbulence model equations. In this study the buoyancy terms are insignificant and not applied.

In the present study both preconditioning and pressure correction methods are used to determine the pressure.

In both methods the flux calculation is a simplified version of the approximate Riemann-solver utilized for compressible flows [1]. It should be noted that in this approach the artificial sound speed affects the solution, but the effect is of a second-order and it should not be visible as the grid is refined. The effect is similar to the Rhie and Chow interpolation method applied in commercial codes. The solution method applied is described in [2].

The pressure correction method used is described in [3]. As compared to the traditional pressure correction methods, the basic difference of the present method is that all the residuals are calculated simultaneously and only once during an iteration cycle. The complexity of the coupled implicit solution is avoided by manipulating the explicit residuals. Since the same explicit stage is used as in preconditioning [2], the pressure correction can be used as a parallel solution method for the preconditioning.

In time-accurate simulations the both precondition and pressure correction methods are used inside a physical time step [4]. Each time step is treated as a steady-state case and iterations are made inside the time step. The time derivative term is treated as a source term. The method is fully implicit and a three-level approximation is used for the time derivative.

3 Turbulence Modelling

3.1 $k-\epsilon$ Model

As mentioned, turbulent stresses resulting from the Reynolds averaging of the momentum equation are modelled by using Boussinesq's approximation (6). The turbulent viscosity coefficient μ_T is determined by using Chien's [5] low-Reynolds number $k-\epsilon$ model from the formula

$$\mu_T = c_\mu \rho \frac{k^2}{\epsilon} \tag{10}$$

where c_μ is a empirical coefficient. The source term of Chien's model is

$$Q = \begin{pmatrix} P - \rho\epsilon - 2\mu\dfrac{k}{y_n^2} \\ c_1\dfrac{\epsilon}{k}P - c_2\dfrac{\rho\epsilon^2}{k} - 2\mu\dfrac{\epsilon}{y_n^2}e^{-y^+/2} \end{pmatrix} \tag{11}$$

where y_n is the normal distance from the wall, and the dimensionless distance y^+ is defined by

$$y^+ = y_n\frac{\rho u_\tau}{\mu} = y_n\frac{\sqrt{\rho\tau_w}}{\mu} \approx y_n\left[\frac{\rho|\nabla\times\vec{V}|}{\mu}\right]_w^{1/2} \tag{12}$$

Here u_τ is friction velocity and τ_w is friction on the wall, and the connection between them is $u_\tau = \sqrt{\tau_w/\rho}$. The unknown production of the turbulent

kinetic energy is modelled using Boussinesq's approximation (6)

$$\begin{aligned} P &= -\overline{\rho u_i'' u_j''}\frac{\partial u_i}{\partial x_j} \\ &= \left[\mu_T(\frac{\partial u_i}{\partial x_j}+\frac{\partial u_j}{\partial x_i}-\frac{2}{3}\delta_{ij}\frac{\partial u_k}{\partial x_k})-\frac{2}{3}\delta_{ij}\rho k\right]\frac{\partial u_i}{\partial x_j} \end{aligned} \tag{13}$$

The turbulence model presented above contains empirical coefficients. Those are given by [1]

$$\begin{aligned} c_1 &= 1.44 & \sigma_k &= 1.0 \\ c_2 &= 1.92(1-0.22e^{-Re_T^2/36}) & \sigma_\epsilon &= 1.3 \\ c_\mu &= 0.09(1-e^{-0.0115y^+}) \end{aligned} \tag{14}$$

where the turbulence Reynolds number is defined as

$$Re_T = \frac{\rho k^2}{\mu\epsilon} \tag{15}$$

Chien's model is very robust, but it has several shortcomings. It usually overestimates the turbulence level and is not performing well in a case of an increasing pressure gradient.

3.2 $k-\omega$ Model

In order to improve the near-wall behaviour of a $k-\varepsilon$ model, a mixture of the $k-\varepsilon$ and $k-\omega$ models, known as Menter's $k-\omega$ SST model [6, 7, 8], has gained increasing popularity in recent years. Menter's $k-\omega$ SST -model is a two-equation turbulence model where the $k-\omega$-model is utilized in a boundary layer and outside that the turbulence is modelled with the $k-\varepsilon$ model. However, the ε-equation is transferred into the ω-equation in order to allow a smooth change between the models. In the SST-model the turbulent stress is limited in a boundary layer in order to avoid unrealistic strain-rates, which are typical of the Boussinesq eddy viscosity models. This model can also be modified in order to take into account the effect of surface roughness. The equations for k and ω are

$$\begin{aligned} \rho\frac{\partial k}{\partial t}+\rho u_j\frac{\partial k}{\partial x_j} &= P-\beta^*\rho k\omega \\ &+ \frac{\partial}{\partial x_j}\left[(\mu+\frac{\mu_T}{\sigma_k})\frac{\partial k}{\partial x_j}\right] \end{aligned} \tag{16}$$

$$\rho\frac{\partial \omega}{\partial t}+\rho u_j\frac{\partial \omega}{\partial x_j} = \frac{\gamma\rho}{\mu_T}P-F_4\beta\rho\omega^2 \tag{17}$$

$$\begin{aligned} &+ \frac{\partial}{\partial x_j}\left[(\mu+\frac{\mu_T}{\sigma_\omega})\frac{\partial \omega}{\partial x_j}\right] \\ &+ 2\rho\frac{1-F_1}{\sigma_{\omega 2}\omega}\frac{\partial k}{\partial x_j}\frac{\partial \omega}{\partial x_j} \end{aligned} \tag{18}$$

Function F_4 is for a rotational and curvature correction [9]. It is defined as

$$F_4 = 1 + \max\left(0, \frac{1}{1+3.6Ri}\right) \tag{19}$$

where Ri is the Richardson number variant defined as

$$Ri = \frac{|\Omega_{ij}|}{|S_{ij}|}\left(\frac{|\Omega_{ij}|}{|S_{ij}|} - 1\right) \tag{20}$$

where the vorticity tensor Ω_{ij} and the strain rate tensor S_{ij} are defined as

$$\Omega_{ij} = \frac{1}{2}\left(\frac{\partial u_i}{\partial x_j} - \frac{\partial u_j}{\partial x_i}\right) \tag{21}$$

$$S_{ij} = \frac{1}{2}\left(\frac{\partial u_i}{\partial x_j} + \frac{\partial u_j}{\partial x_i}\right) \tag{22}$$

where $|\Omega_{ij}| = \sqrt{2\Omega_{ij}\Omega_{ij}}$ and $|S_{ij}| = \sqrt{2S_{ij}S_{ij}}$.

The model coefficients in Eqs. (16) and (17) are obtained from

$$(\sigma_k\ \sigma_\omega\ \beta)^T = F_1\,(\sigma_k\ \sigma_\omega\ \beta)_1^T + (1 - F_1)\,(\sigma_k\ \sigma_\omega\ \beta)_2^T \tag{23}$$

with the following values

$$\begin{array}{lll} \sigma_{k1} = 1.176 & \sigma_{\omega 1} = 2.0 & \beta_1 = 0.075 \\ \sigma_{k2} = 1.0 & \sigma_{\omega 2} = 1.168 & \beta_2 = 0.0828 \end{array}$$

Coefficients κ and β^* have constant values of 0.41 and 0.09. Coefficient γ is calculated from

$$\gamma = \frac{\beta}{\beta^*} - \frac{\kappa^2}{\sigma_\omega\sqrt{\beta^*}} \tag{24}$$

Term P in Eqs. (16) and (17) is the production of turbulent kinetic energy and calculated using the Boussinesq approximation from Eq. (13). The last term in the ω-equation originates from the transformed ϵ-equation and it is called a cross-diffusion term. The switching function which governs the choice between the ω- and the ε-equations is

$$F_1 = \tanh\left(\Gamma^4\right) \tag{25}$$

where

$$\Gamma = \min\left(\max\left(\frac{\sqrt{k}}{\beta^*\omega d}; \frac{500\nu}{\omega d^2}\right); \frac{4\rho\sigma_{\omega 2}k}{CD_{k\omega}d^2}\right) \tag{26}$$

The first term is turbulent length scale divided with the distance from the walls. This ratio is around 2.5 in a logarithmic layer and approach zero in a outer layer. The second term has a value of ≥ 1 only in a viscous sublayer.

The meaning of the third term is to ensure stable behaviour of F_1 when the value of ω in the free stream is small.

$$CD_{k\omega} = \max\left(\frac{2\rho}{\sigma_{\omega 2}\omega}\frac{\partial k}{\partial x_j}\frac{\partial \omega}{\partial x_j}; CD_{k\omega\,\min}\right) \tag{27}$$

where $CD_{k\omega\,\min}$ is lower limit of the cross diffusion term. The main purpose of the switching function is to limit the use of the $k-\omega$ model into the boundary layer region. The switch is naturally a weak point in the model, but it seems to work at least in cases of external flows.

In the original SST-model the eddy viscosity μ_T is defined as

$$\mu_T = \frac{a_1 \rho k}{\max\left(a_1\omega; |\Omega_{ij}|F_2F_3\right)} \tag{28}$$

where $a_1 = 0.31$ and $F_3 = 1$. Function F_3 has been added for a proper modelling fo rough walls and will be described later.

Above term F_2 is a switching function that disables the SST limitation outside the boundary layers. Function F_2 works like function F_1, except its value remains as one farther in the outer boundary layer. It is defined as

$$F_2 = \tanh\left(\Gamma_2^2\right) \tag{29}$$

where

$$\Gamma_2 = \max\left(\frac{2\sqrt{k}}{\beta^*\omega d}; \frac{500\nu}{\omega d^2}\right) \tag{30}$$

In Eq. (28) the lower limit of the nominator is based on Bradshaw's assumption, on which the turbulent shear stress in the boundary layer depends on k as follows:

$$|\rho\overline{u''v''}| = a_1\rho k \tag{31}$$

Thus the traditional Kolmogorov-Prandtl-expression $\mu_T = \rho k/\omega$ is used to the limit

$$\mu_T = \frac{|\rho\overline{u''v''}|}{|\Omega_{ij}|} = \frac{a_1\rho k}{|\Omega_{ij}|} \tag{32}$$

This is called the SST-limitation of μ_T. SST-limitation significantly improves the behavior of the model in boundary layers that have an unfavorable pressure gradients, in such cases the traditional model clearly overestimates the turbulent viscosity.

Recently, the model has been further developed by adding a factor F_3. The meaning of function F_3 is to prevent an activation of the SST-limitation near the rough walls [8, 10]. Function F_3 is defined as

$$F_3 = 1 - \tanh\left[\left(\frac{150\nu}{\omega d^2}\right)^4\right] \tag{33}$$

where d is a distance from the walls.

4 Computational Grids and Boundary Conditions

In this simulation the total number of grid cells in a first (finest) grid level is 1 503 168. There are 875 200 grid cells in an impeller part of the grid and 627 968 in a volute part. On the second grid level the total number of grid cells is 375 792, 218 800 in the impeller part and 156 992 in the volute part, respectively. The surface grid is depicted in Figs. 1 and 2.

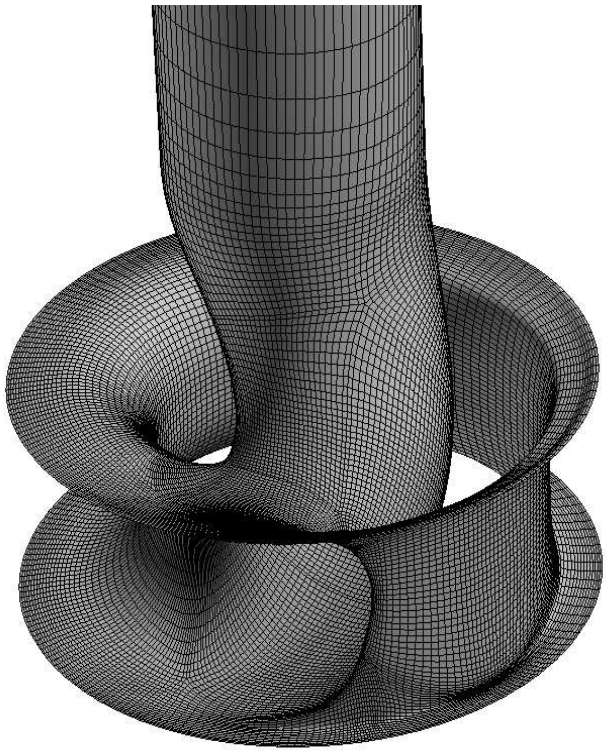

Fig. 1: Surface grid of the impeller.

A quasi-steady simulation is used as an initial guess for a time-accurate simulation. The velocity and turbulent quantities is used as a pump inlet boundary condition and the pressure is given as the pump outlet boundary condition. A value of 800 000 Pa is given for the outlet pressure in order to prevent negative pressures during the iteration. The pressure level is insignificant in a present incompressible case, but the code requires a physically reasonable pressure values. Simulations were made at a design point, where a volume flow has a value of 100 m^3/s or a massflow a value of 27.7 kg/s. Rotational speed is 1475 RPM.

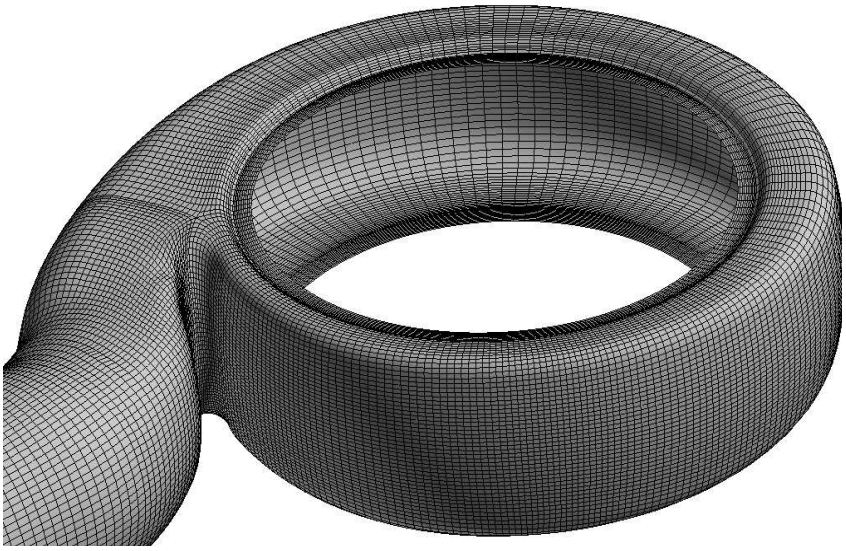

Fig. 2: Surface grid of the volute.

5 Results

With the first level $k-\omega$-simulation two impeller revolutions were simulated with 200 internal iterations, after that time step was changed to correspond a half degree rotation of the impeller for four revolutions. This simulation was used as an initial guess for a simulation with a pressure correction method, where seven impeller rotations using pressure correction with 60 internal iterations were simulated.

With the other simulations than those with the $k-\omega$-model on the first grid level, four impeller revolutions were simulated with 200 internal iterations, after that three revolutions with 400 iterations. Time-step corresponding to one-degree rotation of the impeller was used in these cases. The Courant number of the internal iterations is equal to one in all cases. Multigrid was not used to accelerate convergence in the time-accurate simulations, whereas in the quasi-stedy computations two multi-grid layers were used.

Some convergence histories within a timestep are shown in Figs. 3. The turbulent kinetic energy is fully converged after 150 internal iterations, whereas dissipation of turbulent kinetic energy is behaving a bit strangely. Massflows are constant after first ten iterations.

A head is calculated from

$$H = \frac{p_2 - p_1}{\rho g} \tag{34}$$

where p_1 is the inlet pressure, p_2 the outlet pressure; ρ the density, and g the acceleration due to gravity. The efficiency is obtained from

$$\eta = \Delta E / T\omega \tag{35}$$

where ΔE is the difference between the mechanical energy flux at the inlet and the outlet and $T\omega$ is the required axial power. The axial power should be smaller than the measured one, since several components of the loss, for example the friction on the outside of the impeller and bearing losses, are not taken into account. The time averaged head, efficiency and axial power needed are presented in Table 1.

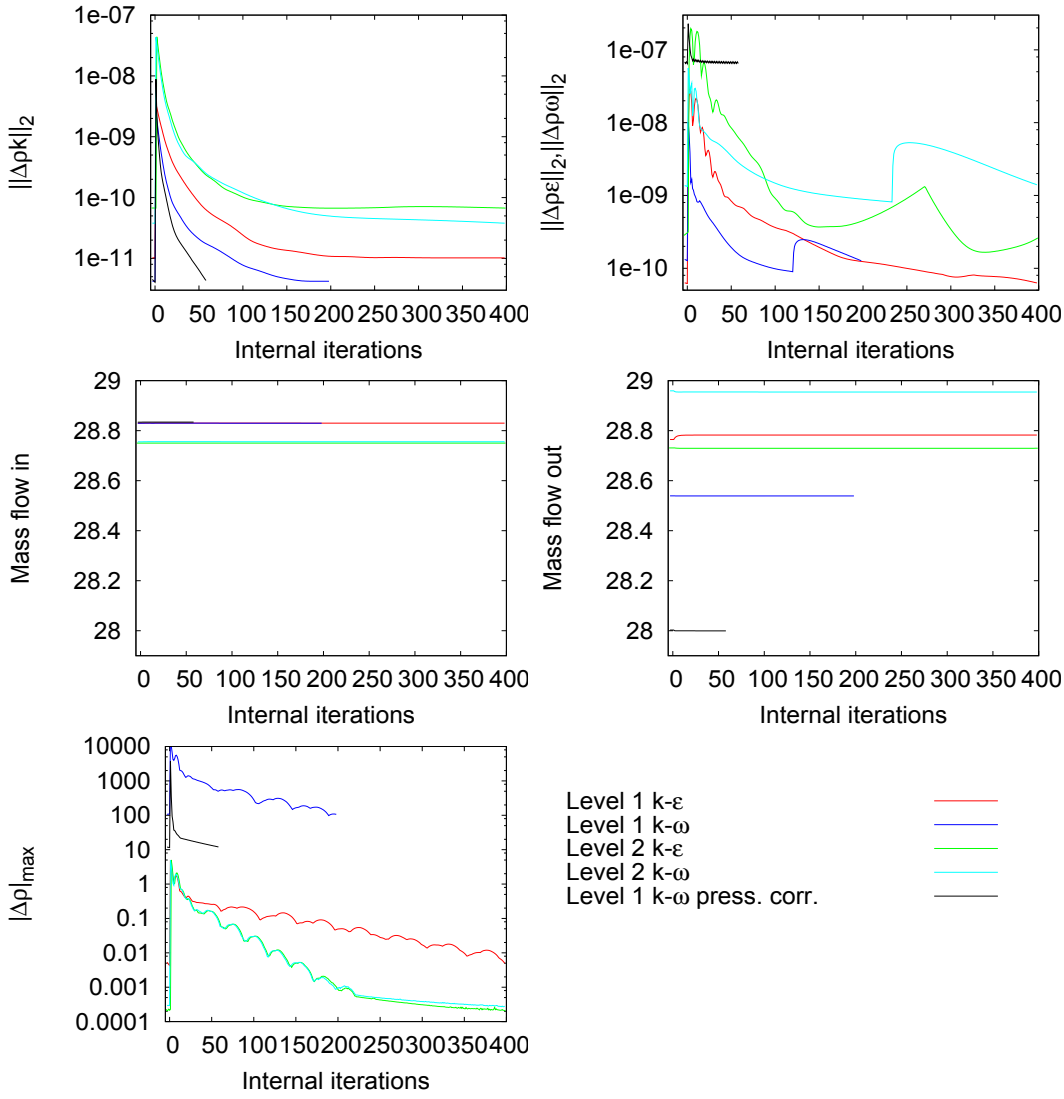

Fig. 3: Convergence histories of the internal iterations within one timestep. Orientation of figures: The $||L||_2$-norm of the turbulent kinetic energy residual (top left), the $||L||_2$-norm of the dissipation of the turbulent kinetic energy residual (ϵ) or specific dissipation rate of turbulent kinetic energy (ω) (top right), massflow in (mid left) and massflow out (mid right) and pressure (bottom left).

Table. 1: Pump performance.

	Case	Total Head	Efficiency	Shaft Power
Preconditioning	$k-\varepsilon$ Level 1	9.65 m	87 %	3087 W
	$k-\omega$ Level 1	9.08 m	89 %	2905 W
	$k-\varepsilon$ Level 2	9.44 m	89 %	2961 W
	$k-\omega$ Level 2	9.41 m	90 %	2932 W
Pressure correction	$k-\omega$ Level 1	9.04 m	89 %	2911 W
Experimental		9.2 m	78 %	3250 W

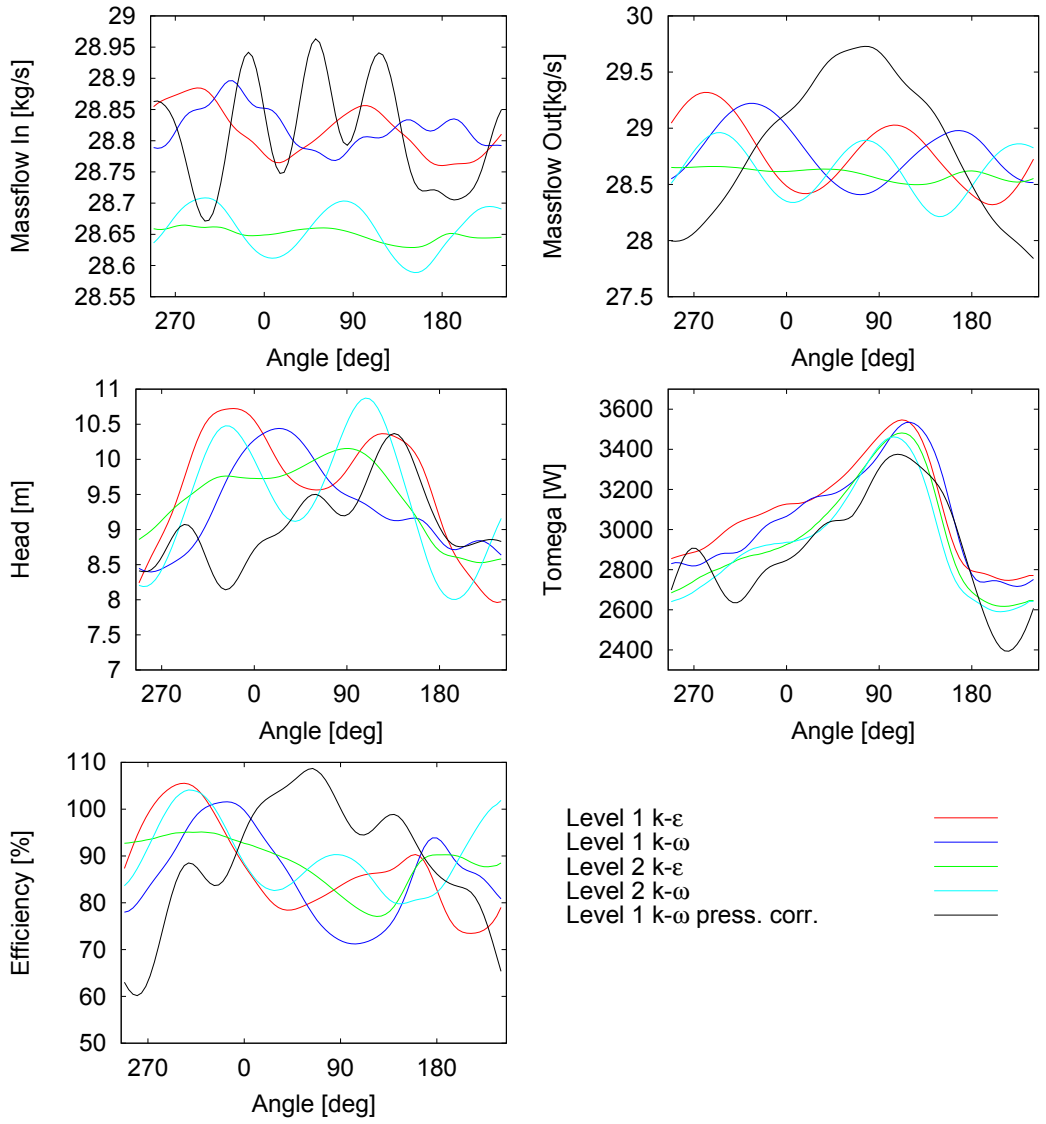

Fig. 4: Massflow in (top left) and massflow out (top right), the head (mid left), the shaft power (mid right) and the efficiency (bottom) as a function of the impeller angle.

The head, mass balance, efficiency and axial power over a one impeller cycle are shown in Fig. 4. Massflow fluctuations are moderate. The inlet massflows oscillate, because the mass flow includes the Rhie-Chow dissipation term

$$\dot{m}_{i+1/2} = S_{i+1/2}\left[\rho\frac{\bar{u}_i + \bar{u}_{i+1}}{2} - \frac{C}{\dot{m}_\infty}(p^r - p^l)\right] \tag{36}$$

where p^r and p^l are pressure on both sides of the cell wall $i+1/2$, $\dot{m}_\infty$ is a reference massflow and $C \approx 0.1$ a parameter. The reason for the outlet massflow deviations from the inlet value is unknown. Peaks in the head curve take place at a different place of impeller rotation cycle, indicating that reflections from boundary condition is affecting the pressure field. The efficiency and massflow curves of pressure correction method are very different from the others.

The problem of fluctuating pressure is related to convergence problems. When a number of internal iterations is increased, pressure is changing linear after first 50 iterations. Same kind of behaviour is also seen in a simulation with the pressure correction method. Convergence histories of an average pressure within a timestep for first level $k-\omega$ case both preconditioning and the pressure correction methods are shown in Fig. 5.

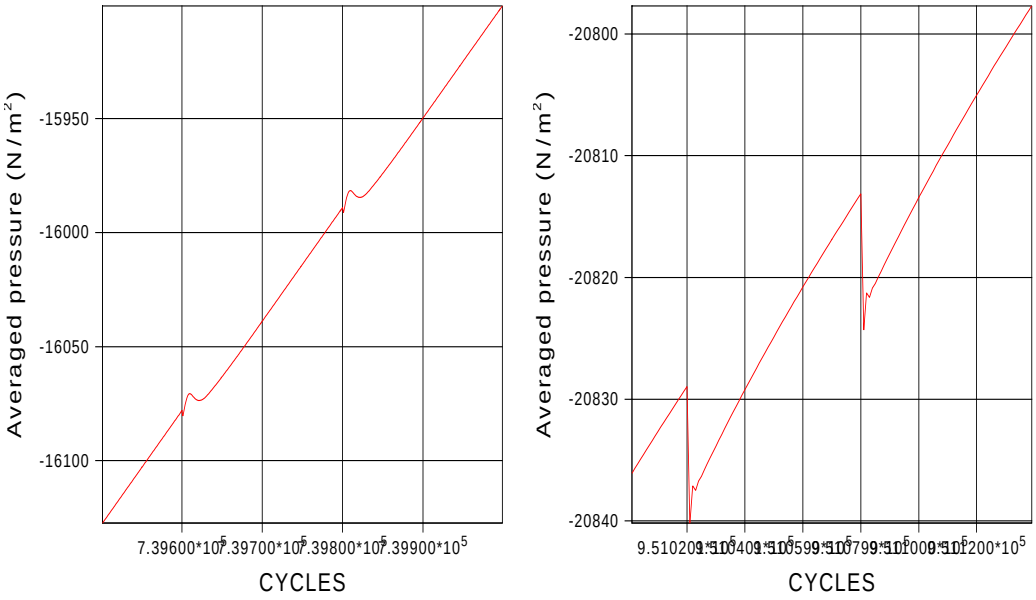

Fig. 5: Convergence history of a average pressure within a timestep. The precondition method on the left and the pressure correction method on the right.

Velocity distributions at measurement stations 1 and 3, given in Fig. 6, are shown in Figs. 8 – 9. Definition of a impeller position 0° is shown in Fig. 7. In the velocity distributions, there are no significant differences between cases. In the radial velocity curves around a distance of 0.07 m curve shapes are different from the measurements. It is possible that the solution in that area is affected by the simplification of the geometry. Any way the pulse like behaviour in the radial velocity distribution is visible in related animations both in measurements and simulations.

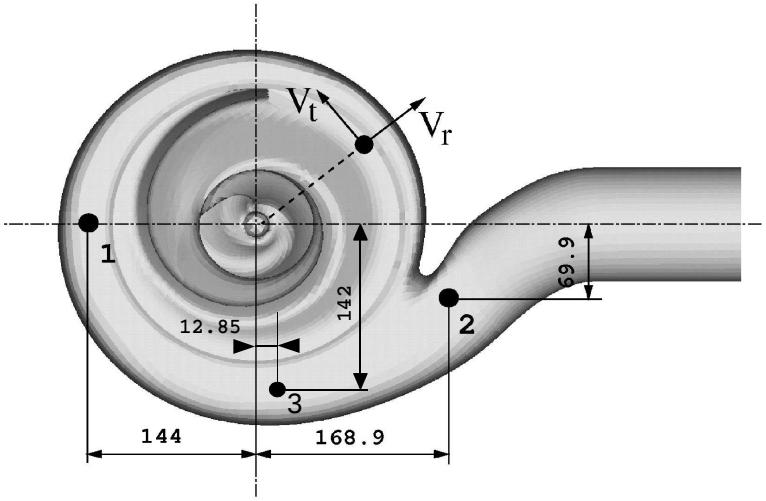

Fig. 6: Locations of the measurement points and directions of the tangential and radial velocities.

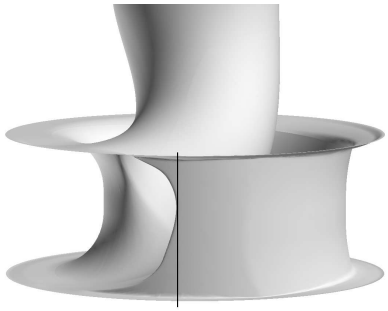

Fig. 7: Impeller angle is 0° when tip of the impeller blade is passing a plane from measurement point 1 to center of the impeller.

Distributions for the velocity, pressure and turbulent kinetic energy, taken on a plane at a distance of 40 mm from the bottom of the impeller, are shown in Figs. A-1 – A-12 of appendix A. The velocity in the figures is in an inertial coordinate system. In the velocity distributions there are only small differences, but in the pressure distributions differences are significant, as one can assume by looking a head curve in Fig. 4. In turbulent kinetic energy distributions $k-\omega$ simulations yields much larger values and especially in the pressure condition case.

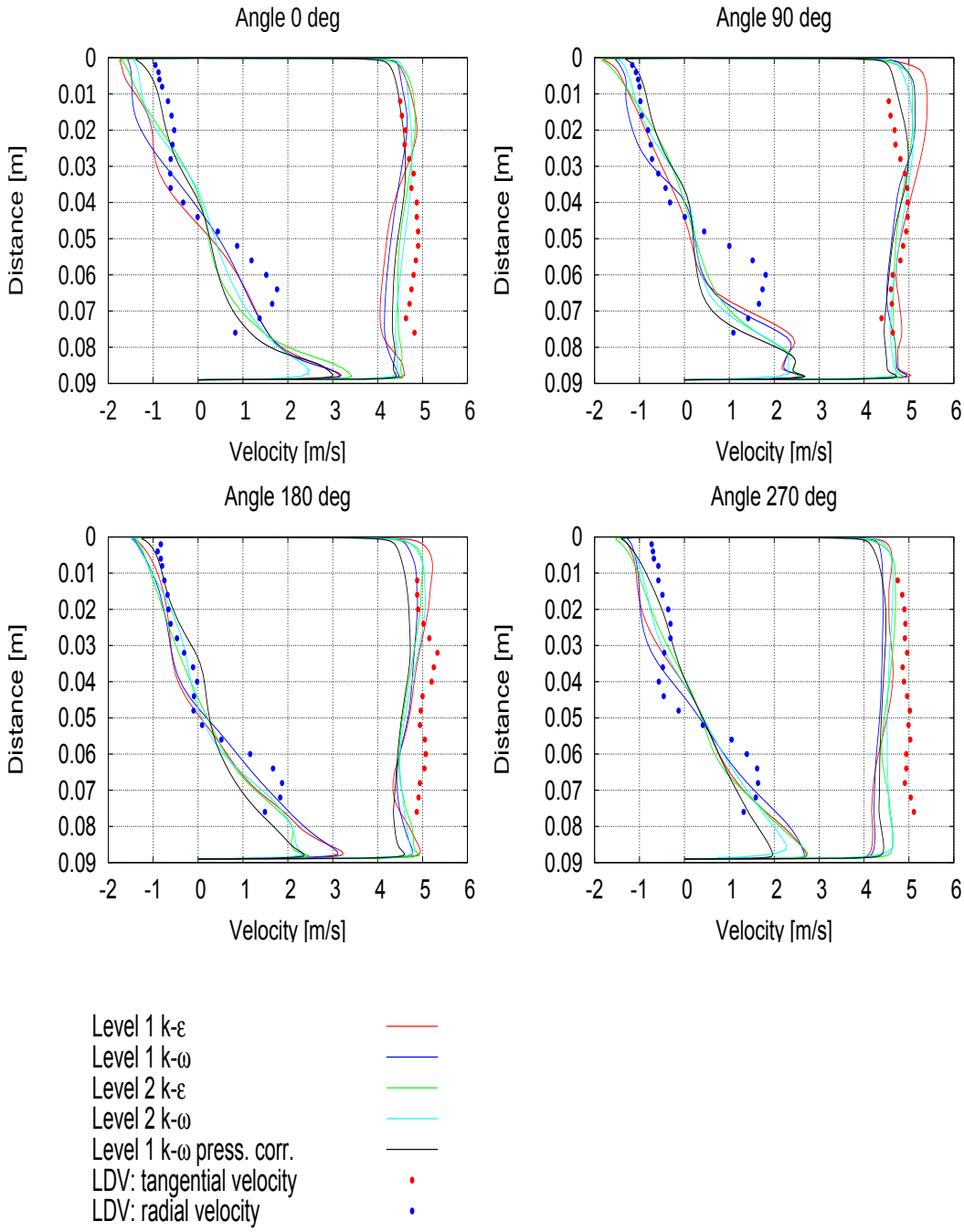

Fig. 8: Velocity distributions at measurement point 1.

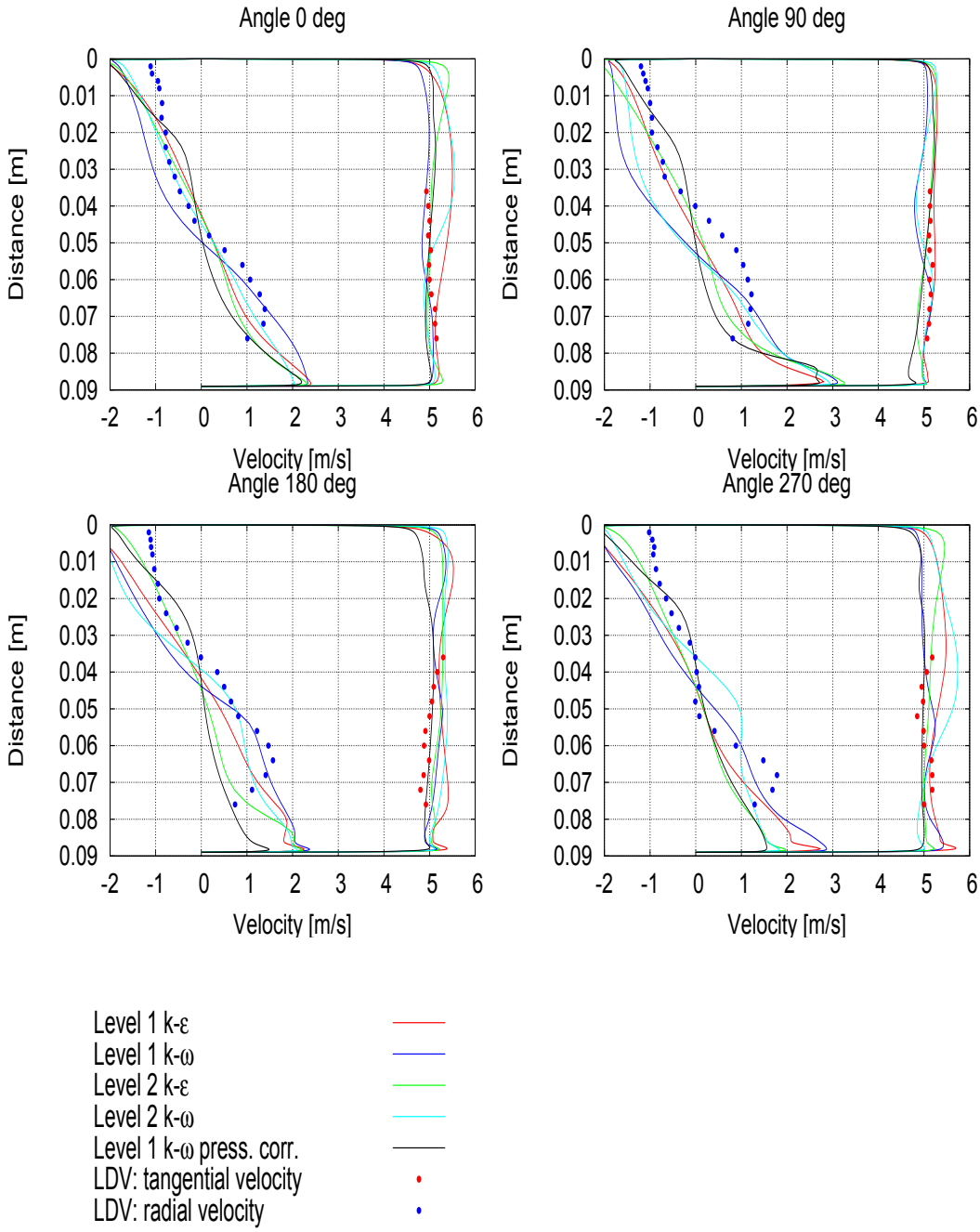

Fig. 9: Velocity distributions at measurement point 3.

6 Discussion

In this study a single-blade sewage pump is simulated numerically using a low-Reynolds number $k-\epsilon$ and $k-\omega$ turbulence closures. Also different solution approach, precondition and pressure correction methods were utilized.

Same pressure fluctuation problem discussed in [11] is still present, even it was thought that the extremely good quality grid and a much less pulsating flow was assumed to solve the problem. The effect to the pump performance is, however, much smaller.

The average performance prediction is quite good remembering that axial power should be smaller than the measured one, since several components of the loss, for example the friction on the outside of the impeller and bearing losses, are not taken into account. Time-accurate prediction of the pump performance if quite different between the cases, which makes results unreliable. Largest differences in head and efficiency results are between pressure correction method and all precondition method simulations. Pressure levels are influenced by grid density, where as the turbulent kinetic energy by the turbulence model. With the pressure correction method the pressure is in different phase with the others and turbulent kinetic energy is even than in the other $k-\omega$-simulations. The shaft power is predicted same way in all simulations. As compared to the predicted pressure, velocity distributions are predicted with quite good accuracy.

References

[1] *FINFLO User Guide, version 7.1.* Helsinki University of Technology, Finland, 2003.

[2] Rahman, M., Siikonen, T., and Miettinen, A., "A pressure-correction method for solving fluid flow problems on a collocated grids," *Numerical Heat Transfer, Part B*, Vol. 32, 1997, pp. 63–84.

[3] Siikonen, T., "Developments in Pressure Correction Methods for a Single and Two Phase Flow CFD/MECHA-10-2010," Aalto University, Department of Applied Mechanics, 2010.

[4] Hoffren, J., "A Numerical Method for Simulating Unsteady Flow Including Solid/Fluid Interaction," Helsinki University of Technology, Laboratory of Aerodynamics, 1995. ISBN 951–22–2759–2.

[5] Chien, K.-Y., "Predictions of Channel and Boundary-layer Flows with a Low-Reynolds-Number Turbulence Model," *AIAA Journal*, Vol. 20, No. 1, 1982, pp. 33–38.

[6] Menter, F., "Zonal Two Equation $k-\omega$ Turbulence Models for Aerodynamic Flows," in *24th AIAA Fluid Dynamics Conference*, AIAA, 1993. AIAA Paper 93–2906.

[7] Menter, F., "Two-Equation Eddy-Viscosity Turbulence Models for Engineering Applications," *AIAA Journal*, Vol. 32, No. 8, 1994, pp. 1598–1605.

[8] Hellsten, A. and Laine, S., "Extension of the $k-\omega$ Shear-Stress Transport Turbulence Model for Rough-Wall Flows," *AIAA Journal*, Vol. 36, No. 9, 1998, pp. 1728–1729.

[9] Hellsten, A., "Some improvements in Menter's $k-\omega$ SST turbulence model," in *29th AIAA Fluid Dynamics Conference*, (Albuquerque, New Mexico, USA), AIAA paper 98–2554, 1998.

[10] Hellsten, A. and Laine, S., "Extension of the $k-\omega$-SST Turbulence Model for Flows over Rough Surfaces," in *1997 AIAA Atmospheric Flight Mechanics Conference*, (New Orleans, Louisiana), pp. 252–260, Aug 1997. AIAA Paper 97–3577–CP.

[11] Ala-Juusela, J., "Study of Simulation Parameters and Flow Controlled Boundary Conditions in Single-Blade Pump Simulation, CFD/MECHA-7-2010," Aalto University, Department of Applied Mechanics, 2010.

A Distributions

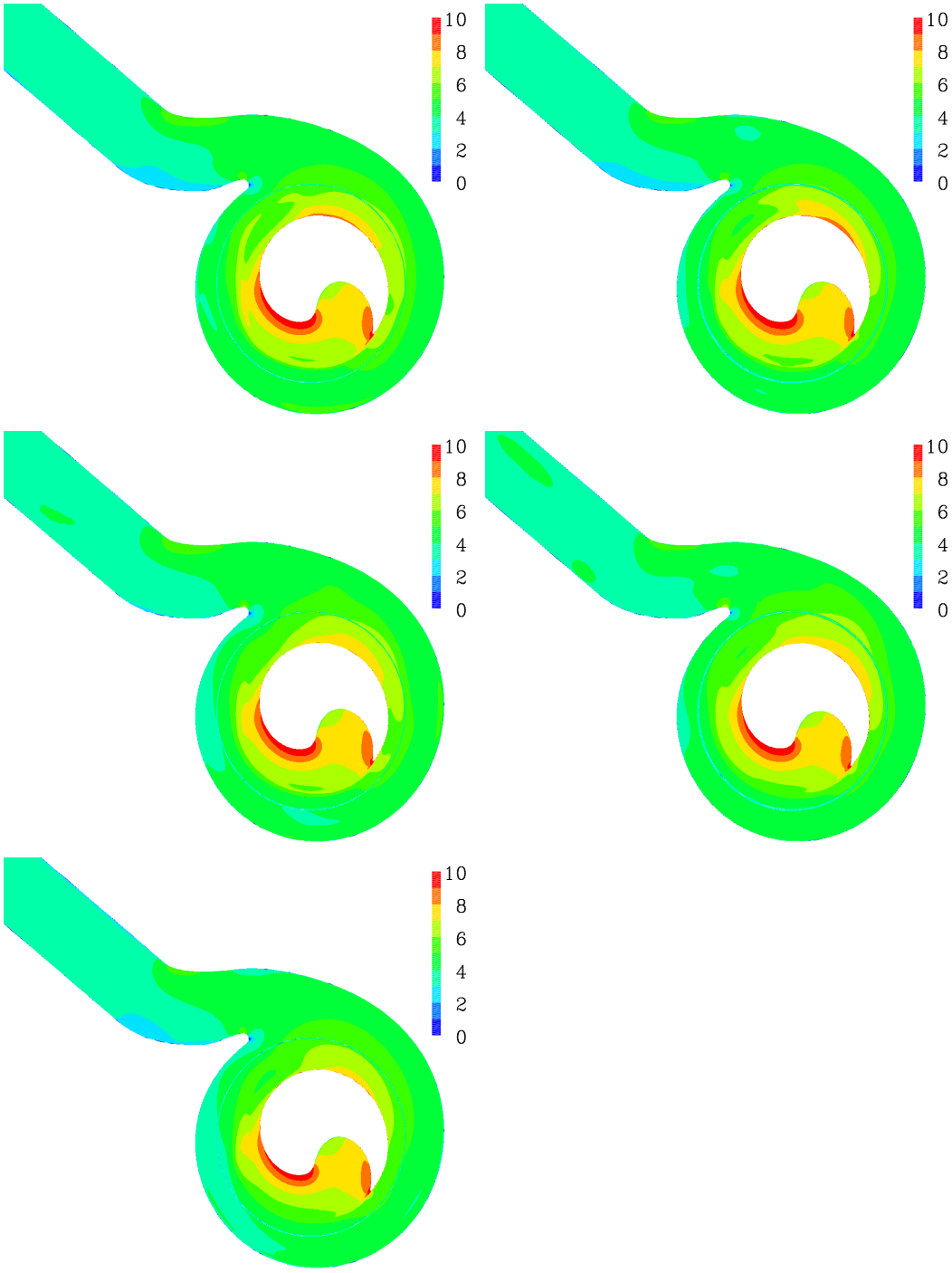

Fig. A-1: Velocity distribution at plane 40 mm from the bottom of the impeller. Top row: Level 1 and level 2 $k-\varepsilon$, mid row: Level 1 and level 2 $k-\omega$, and bottom: Level 1 $k-\omega$ pressure correction case. The angle is 0°.

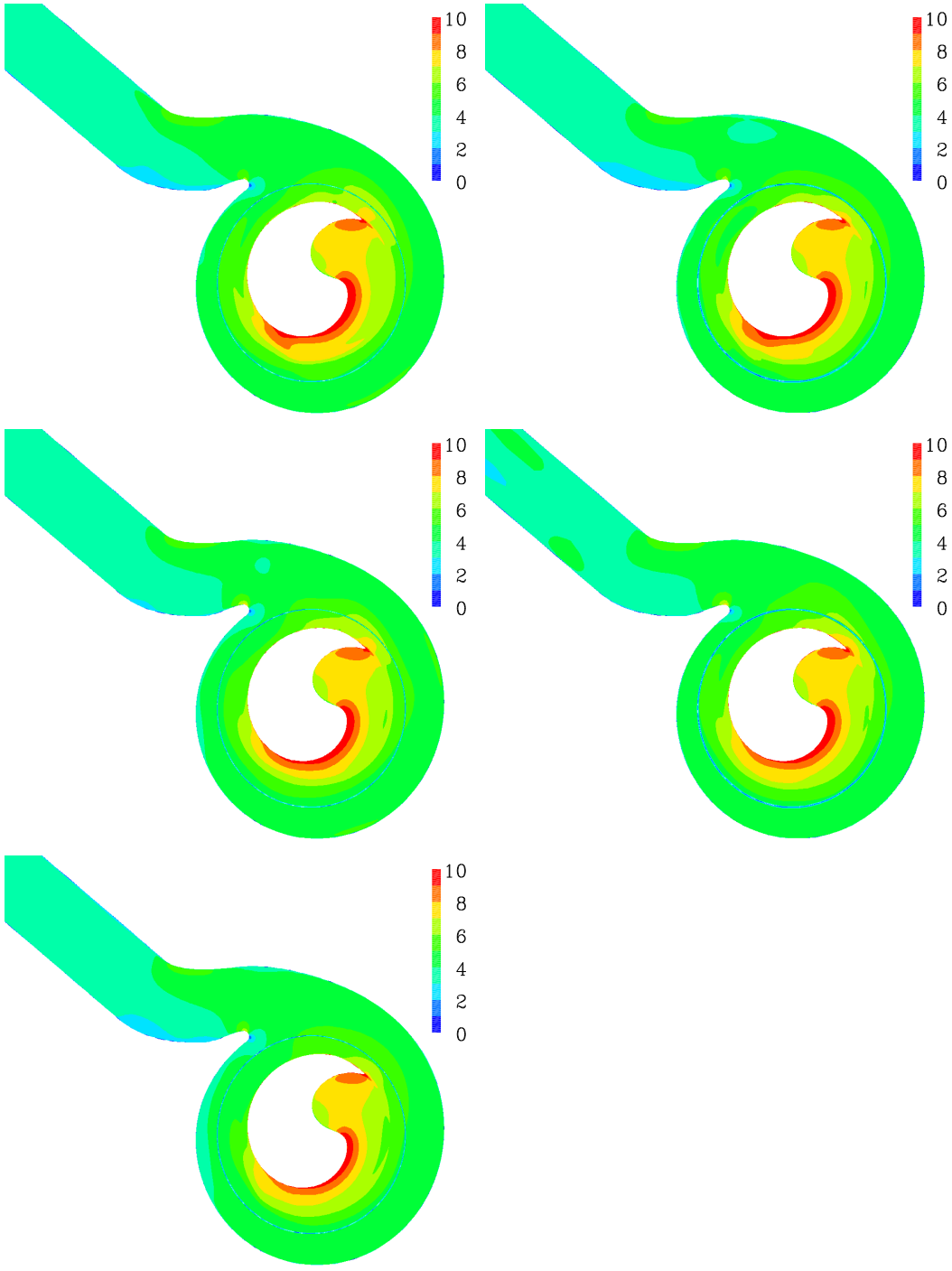

Fig. A-2: Velocity distribution at plane 40 mm from the bottom of the impeller. The orientation as in Fig. A-1. The angle is 90°.

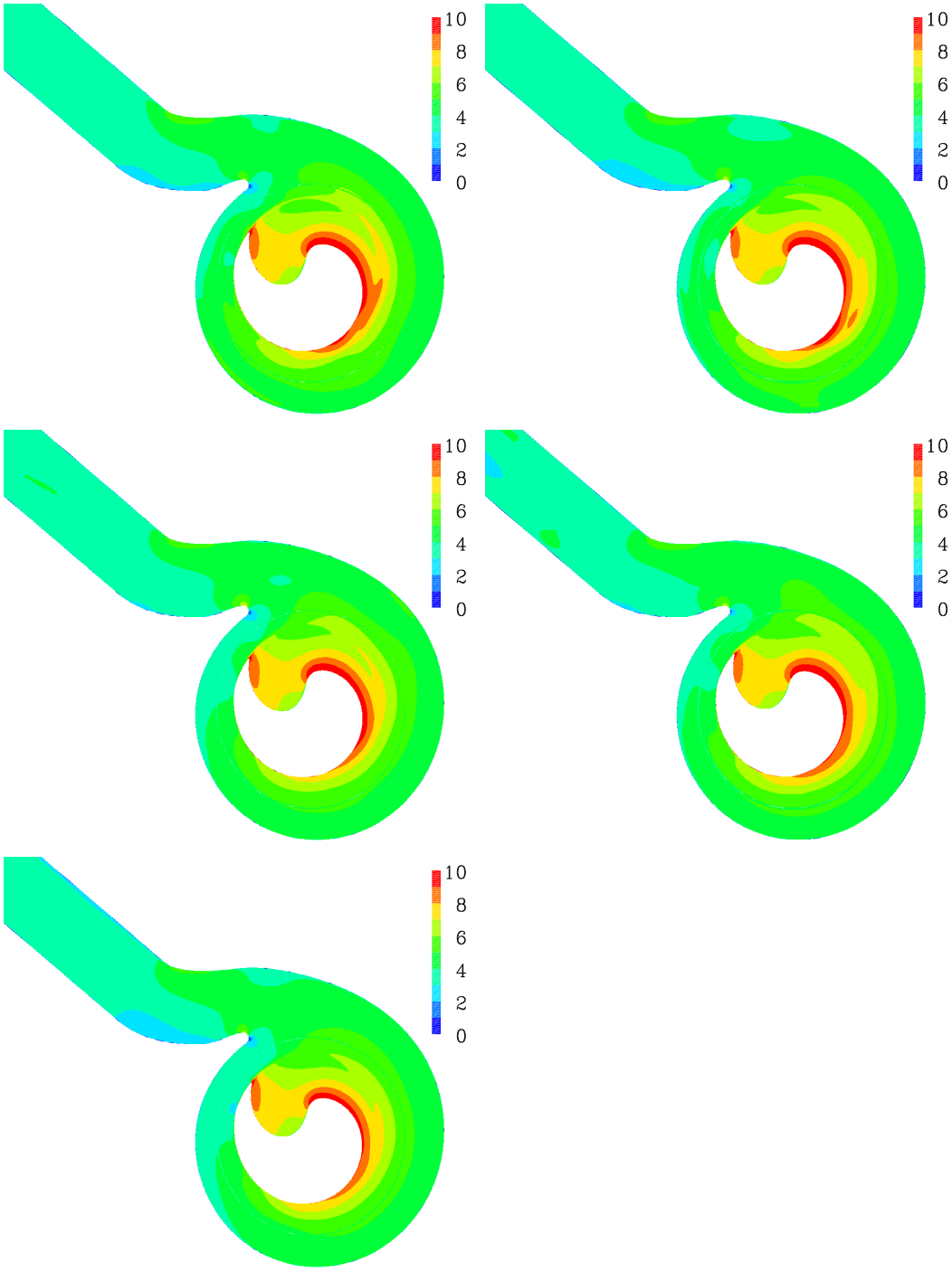

Fig. A-3: Velocity distribution at plane 40 mm from the bottom of the impeller. The orientation as in Fig. A-1. The angle is 180°.

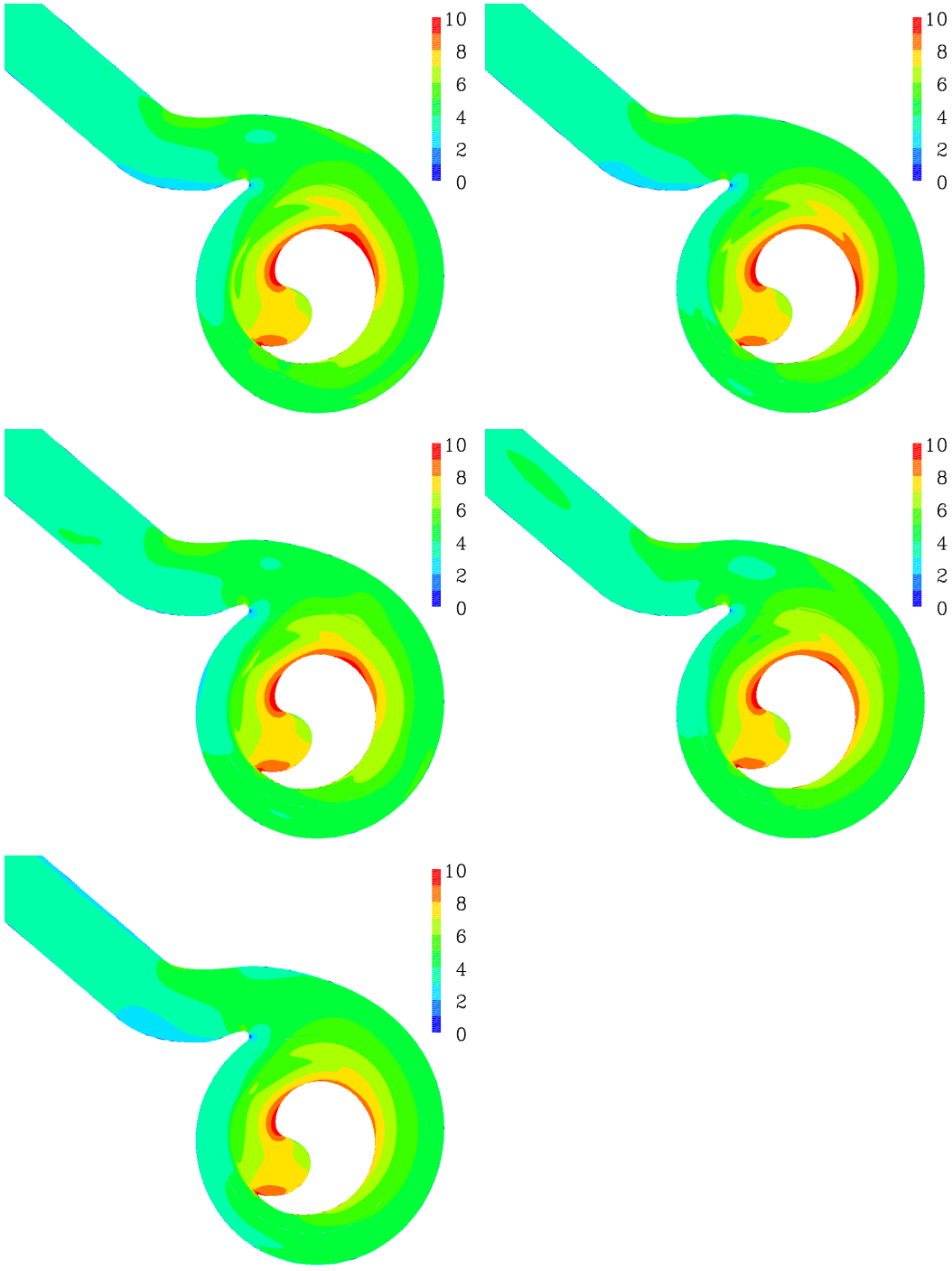

Fig. A-4: Velocity distribution at plane 40 mm from the bottom of the impeller. The orientation as in Fig. A-1. The angle is 270°.

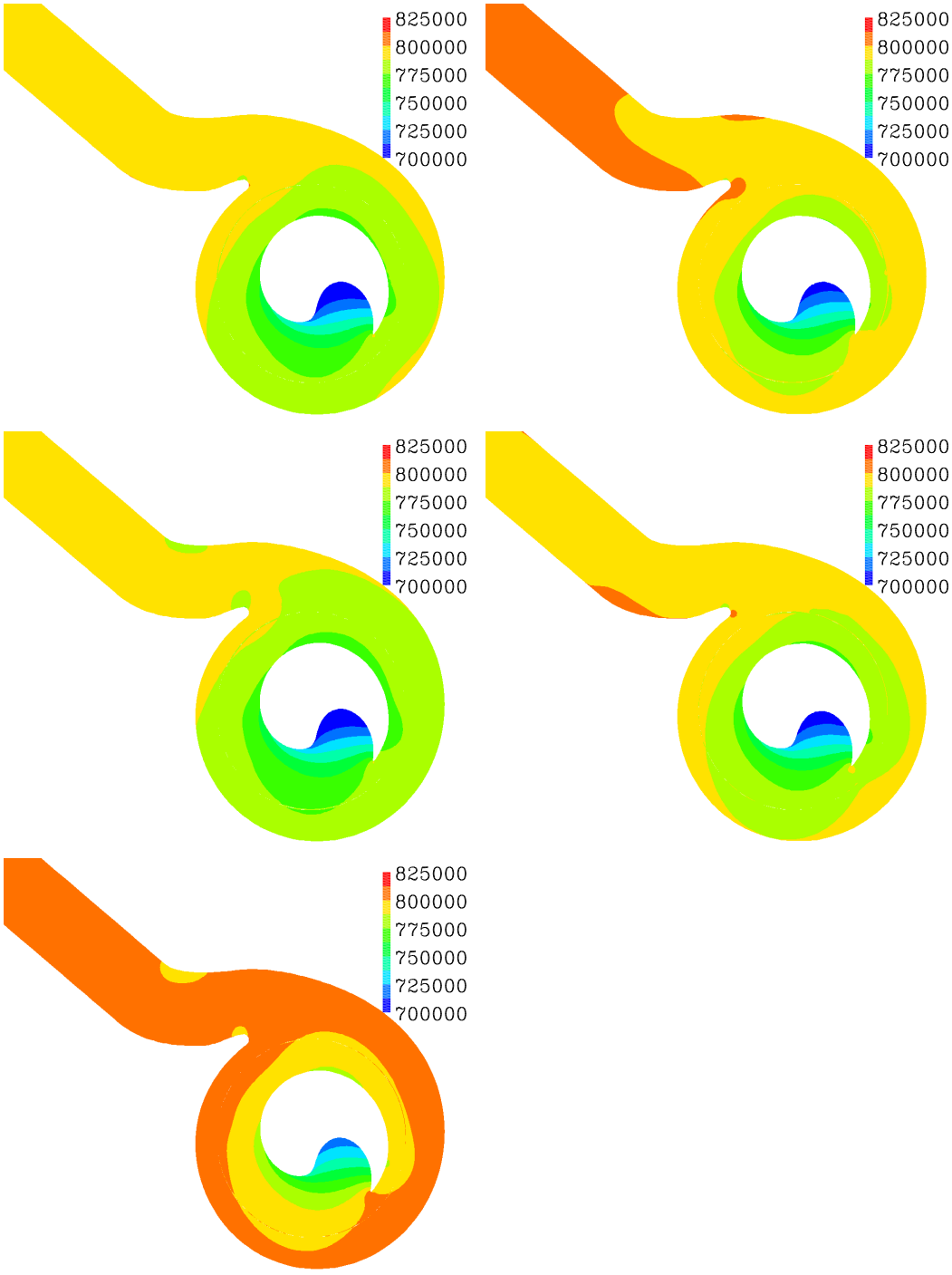

Fig. A-5: Pressure distribution at plane 40 mm from the bottom of the impeller. Top row: Level 1 and level 2 $k-\varepsilon$, mid row: Level 1 and level 2 $k-\omega$, and bottom: Level 1 $k-\omega$ pressure correction case. The angle is 0°.

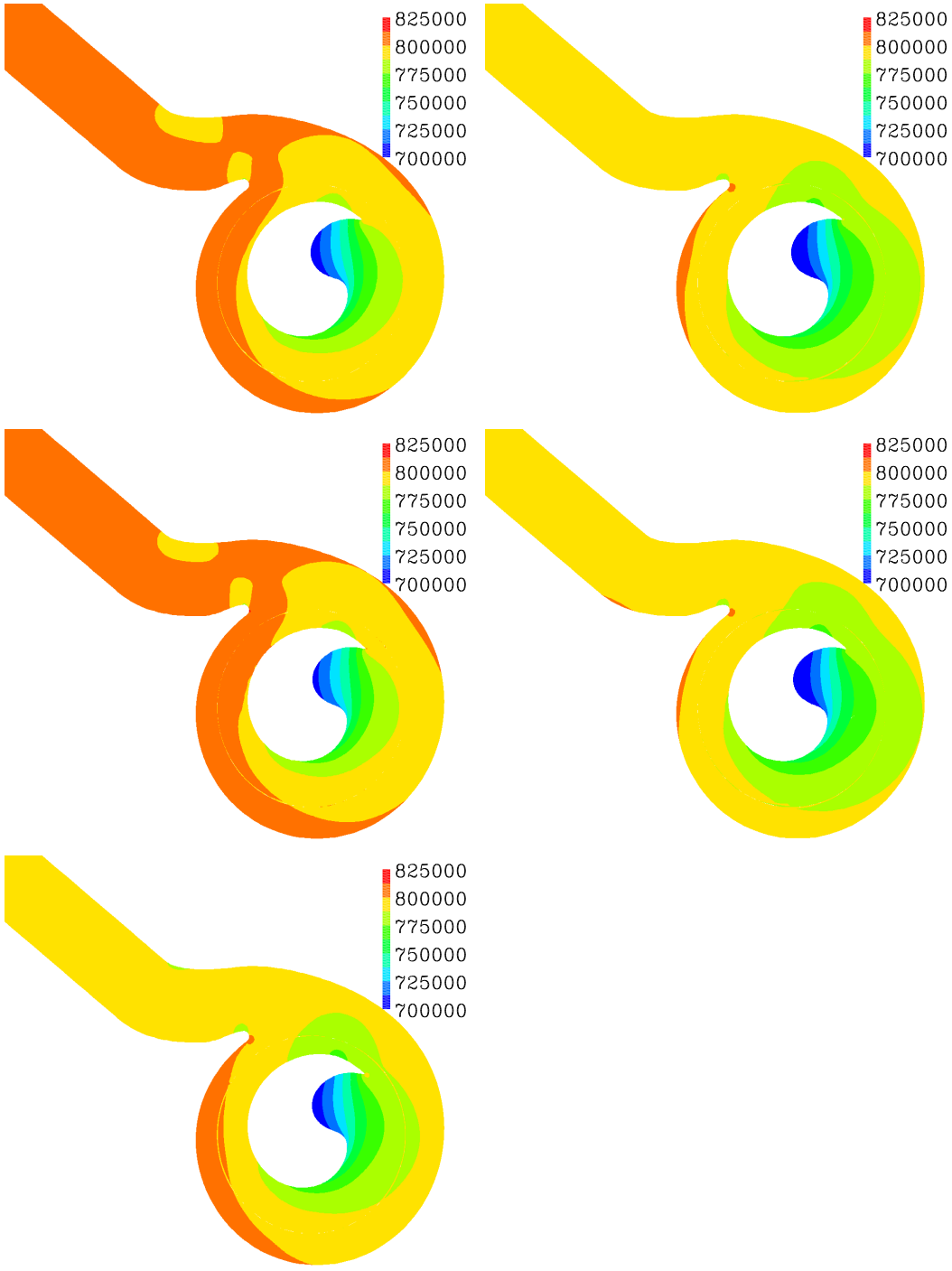

Fig. A-6: Pressure distribution at plane 40 mm from the bottom of the impeller. The orientation as in Fig. A-5. The angle is 90°.

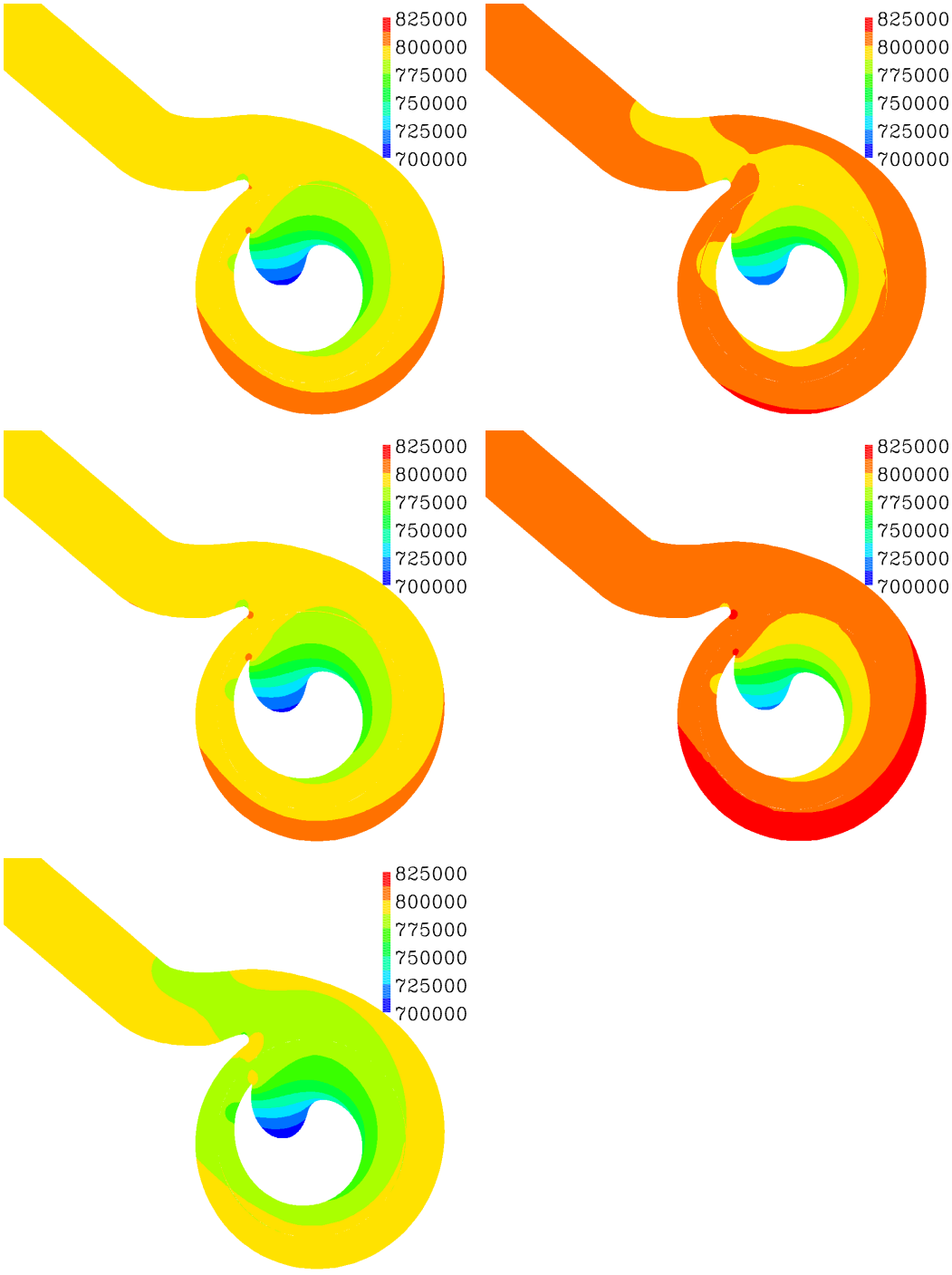

Fig. A-7: Pressure distribution at plane 40 mm from the bottom of the impeller. The orientation as in Fig. A-5. The angle is 180°.

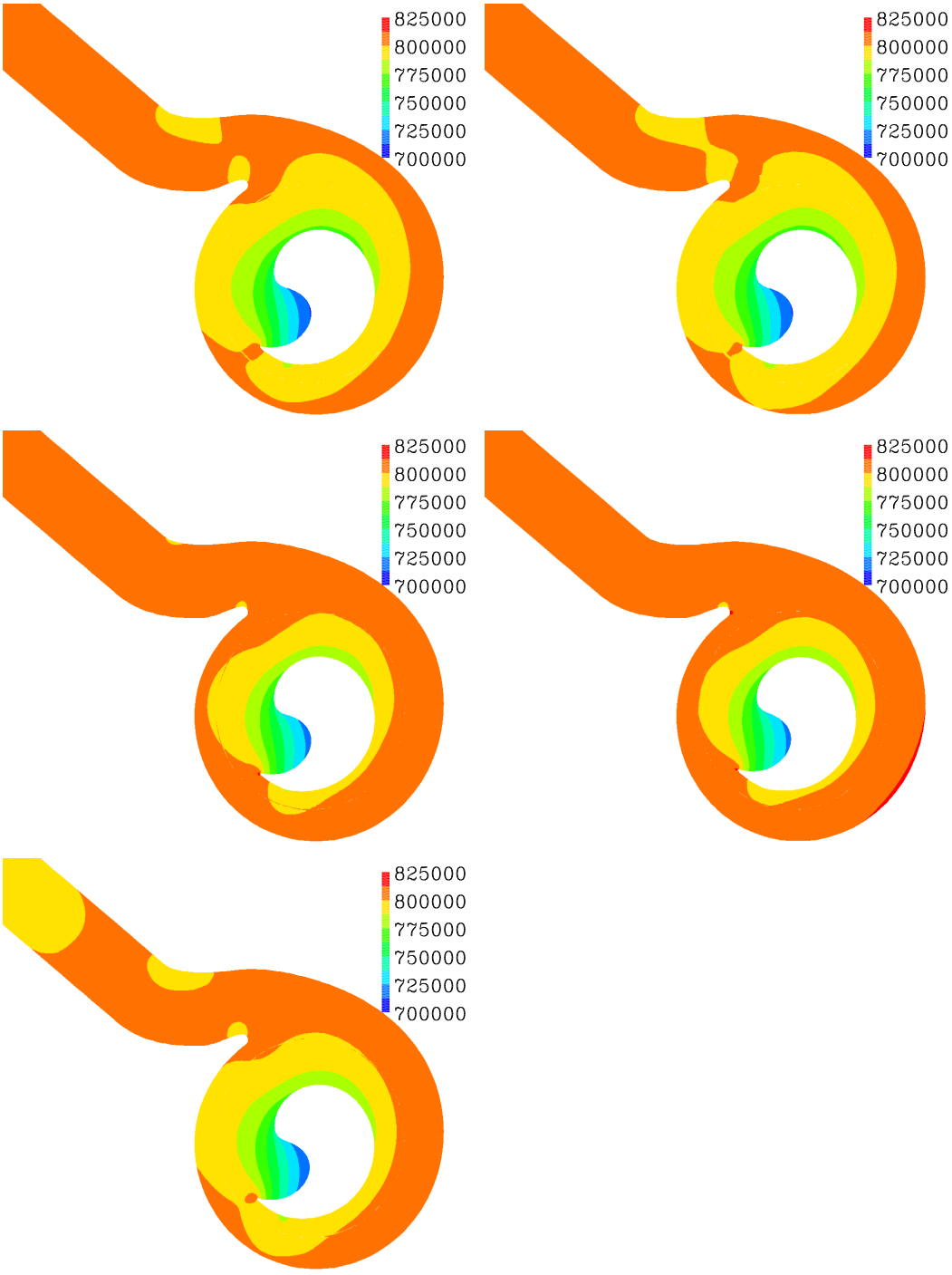

Fig. A-8: Pressure distribution at plane 40 mm from the bottom of the impeller. The orientation as in Fig. A-5. The angle is 270°.

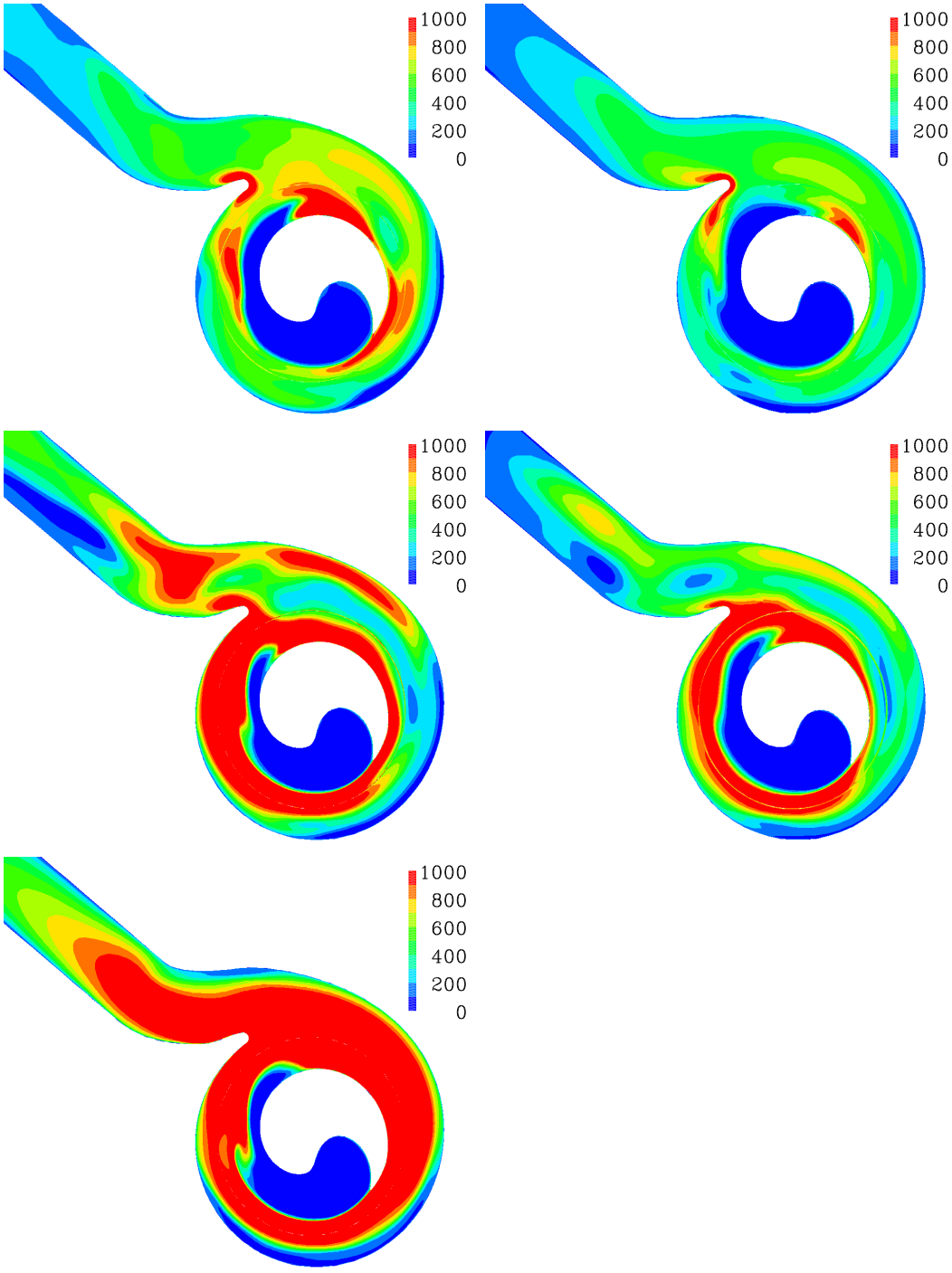

Fig. A-9: Distribution of turbulent kinetic energy (ρk) at plane 40 mm from the bottom of the impeller. Top row: Level 1 and level 2 $k-\varepsilon$, mid row: Level 1 and level 2 $k-\omega$, and bottom: pressure correction case. The angle is 0°.

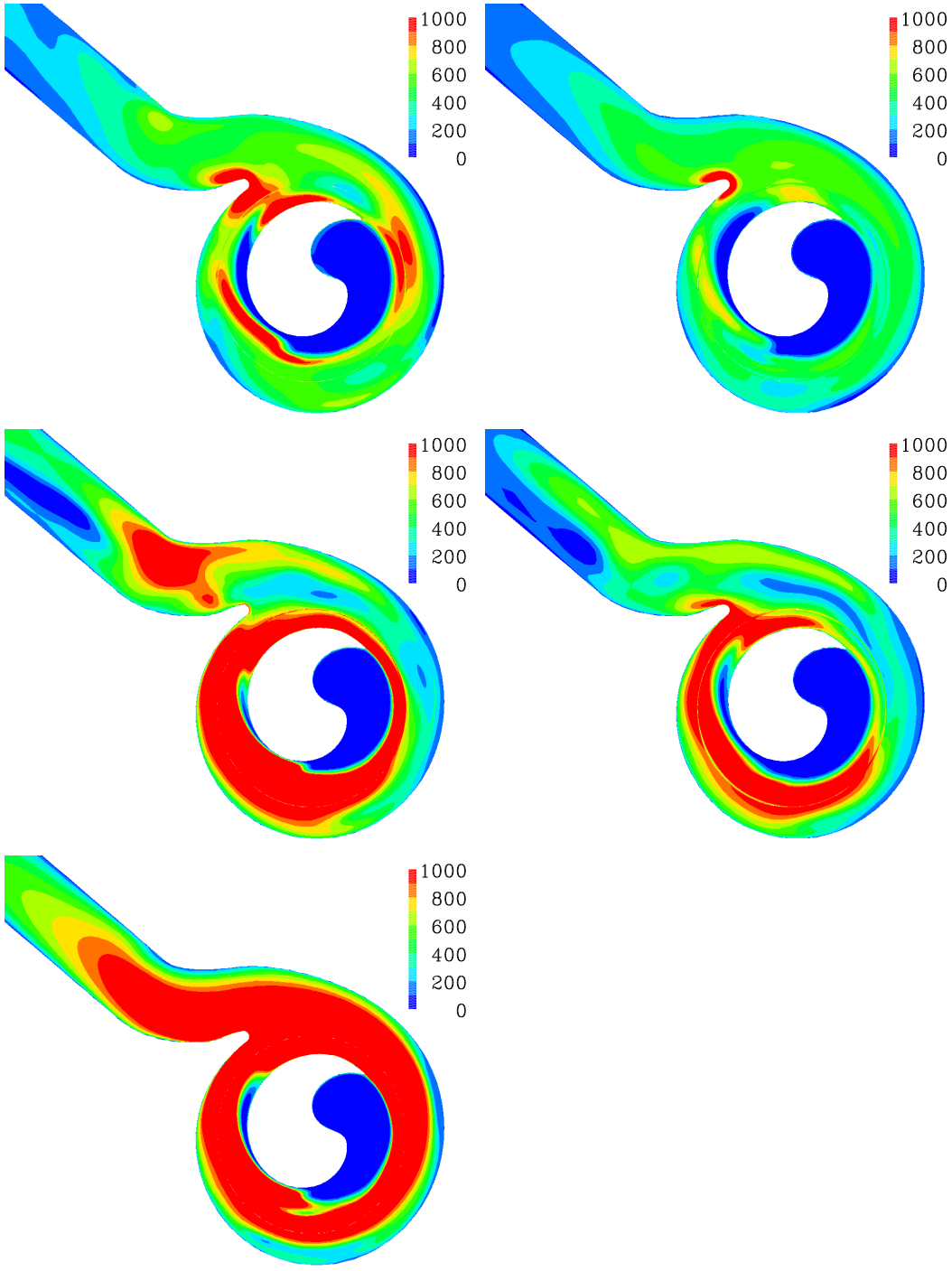

Fig. A-10: Distribution of turbulent kinetic energy (ρk) at plane 40 mm from the bottom of the impeller. The orientation as in Fig. A-9. The angle is 90°.

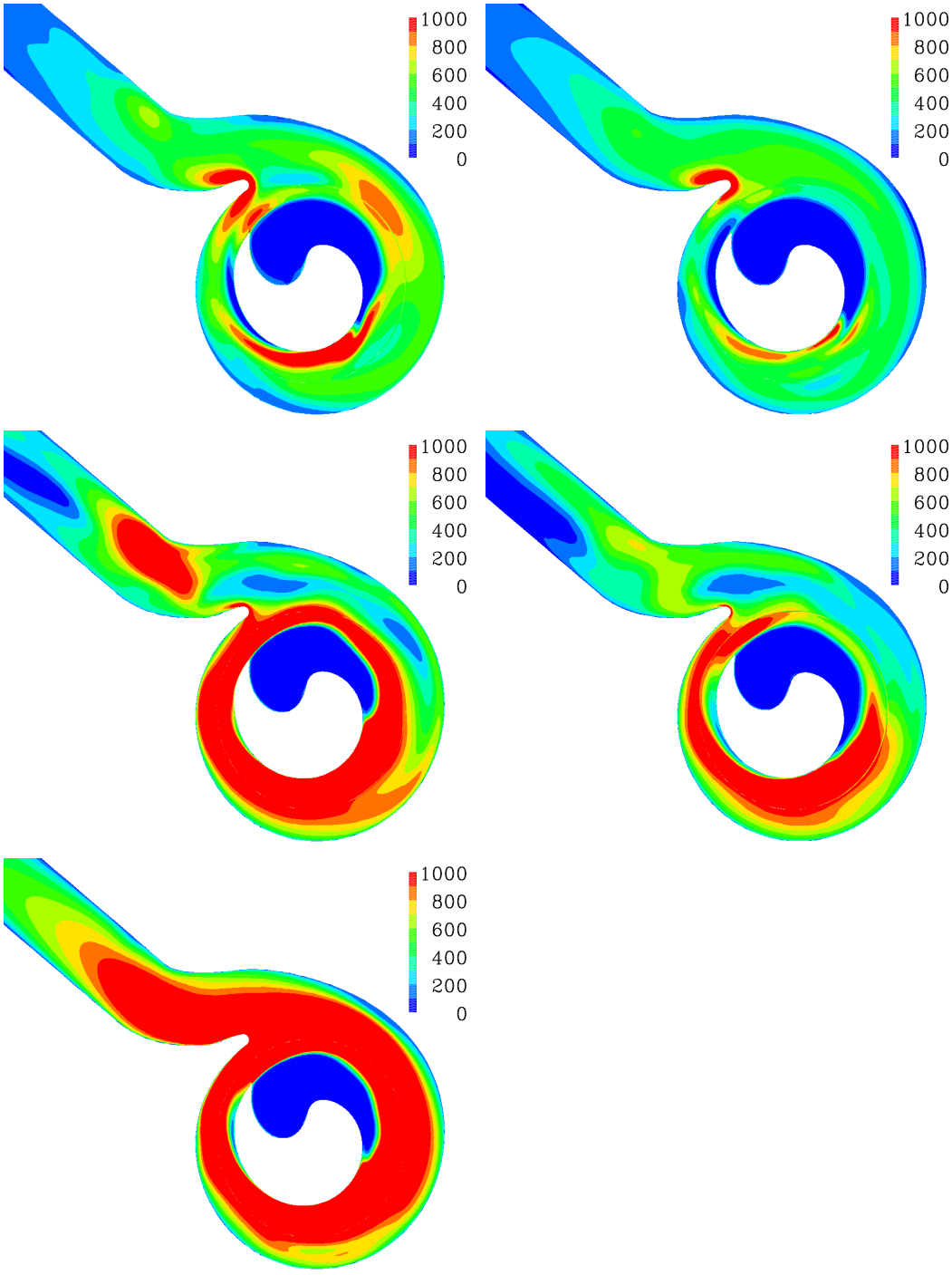

Fig. A-11: Distribution of turbulent kinetic energy (ρk) at plane 40 mm from the bottom of the impeller. The orientation as in Fig. A-9. The angle is 180°.

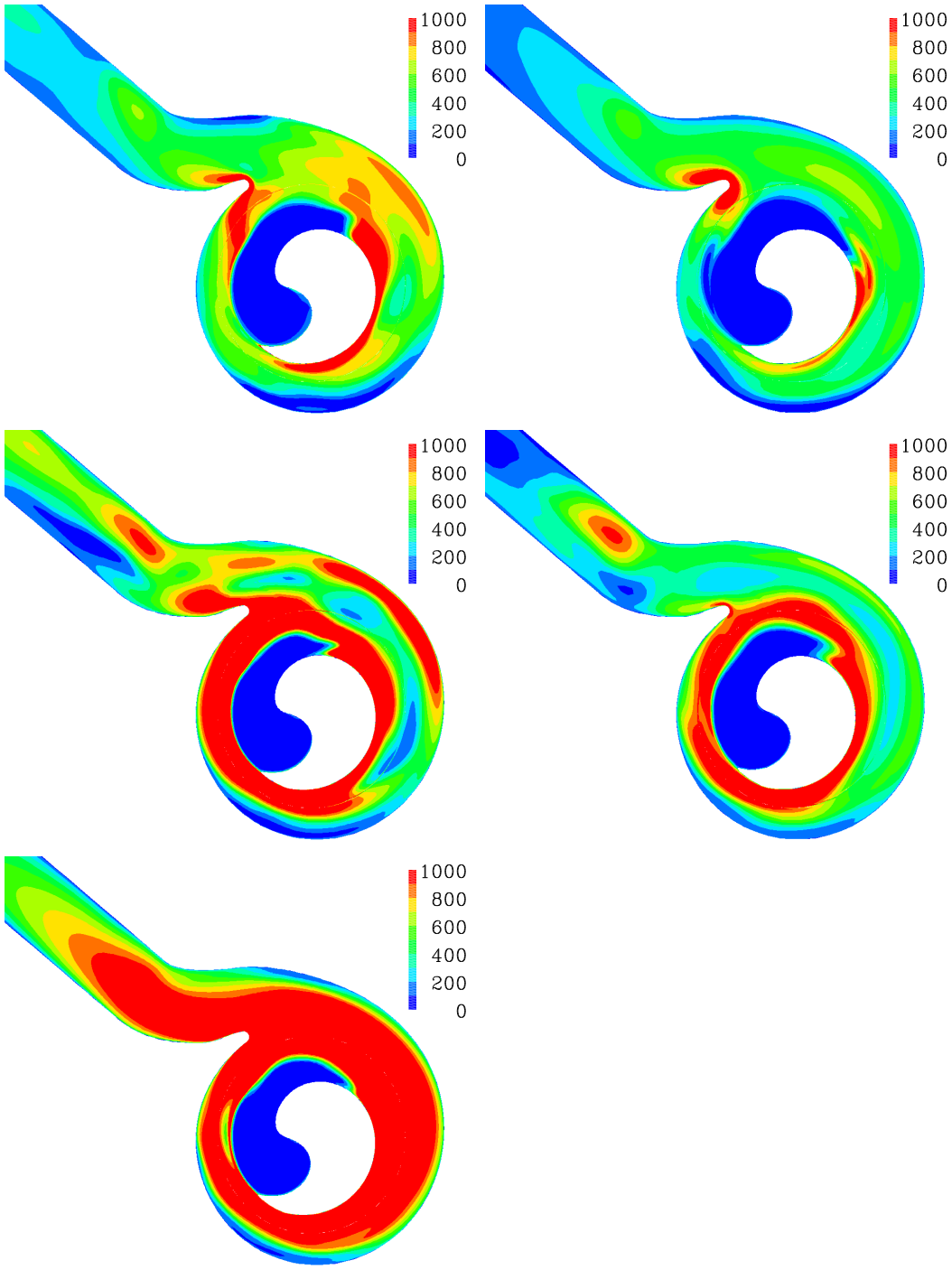

Fig. A-12: Distribution of turbulent kinetic energy (ρk) at plane 40 mm from the bottom of the impeller. The orientation as in Fig. A-9. The angle is 270°.